






RESEARCH ARTICLE | JUNE 04 2024

Effect of a fixed downstream cylinder on the flow-induced vibration of an elastically supported primary cylinder

Junlei Wang  ; Shenfang Li; Daniil Yurchenko  ; Hongjun Zhu  ; Chandan Bose  



Physics of Fluids 36, 063602 (2024)

<https://doi.org/10.1063/5.0207136>



Articles You May Be Interested In

Flow-induced vibrations of a circular cylinder positioned upstream of a fixed cylinder

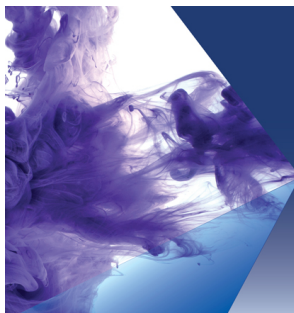
Physics of Fluids (August 2024)

Splitter-plate proximity-induced transitions in flow-induced vibration of a triangular prism

Physics of Fluids (June 2024)

Numerical analysis of reverse wake-induced vibration at low Reynolds number

Physics of Fluids (July 2023)



Physics of Fluids

Special Topic:

Recent Advances in Fluid Dynamics and its Applications

Guest Editors: B.Reddappa, B. Rushi Kumar, Sreedhara Rao Gunakala, Bijula Prabhakar Reddy

[Submit Today!](#)

Effect of a fixed downstream cylinder on the flow-induced vibration of an elastically supported primary cylinder

Cite as: Phys. Fluids **36**, 063602 (2024); doi: 10.1063/5.0207136

Submitted: 6 March 2024 · Accepted: 17 May 2024 ·

Published Online: 4 June 2024



View Online



Export Citation



CrossMark

Junlei Wang,¹  Shenfang Li,¹ Daniil Yurchenko,²  Hongjun Zhu,³  and Chandan Bose^{4,a)} 

AFFILIATIONS

¹School of Mechanical and Power Engineering, Zhengzhou University, Zhengzhou 450000, China

²Institute of Sound and Vibration Research, University of Southampton, Southampton SO17, United Kingdom

³State Key Laboratory of Oil and Gas Reservoir Geology and Exploitation, Southwest Petroleum University, Chengdu 610500, China

⁴Aerospace Engineering, School of Metallurgy and Materials, The University of Birmingham, Birmingham B15 2TT, United Kingdom

^{a)} Author to whom correspondence should be addressed: c.bose@bham.ac.uk

ABSTRACT

This paper numerically investigates the influence of a fixed downstream control cylinder on the flow-induced vibration of an elastically supported primary cylinder. These two cylinders are situated in a tandem arrangement with small dimensionless center-to-center spacing (L/D , L is the intermediate spacing and D is the cylinder diameter). The present two-dimensional (2D) simulations are carried out in the low Reynolds number (Re) regime. The primary focus of this study is to reveal the underlying flow physics behind the transition from vortex-induced vibration to galloping in the response of the primary cylinder due to the presence of another fixed downstream cylinder. Two distinct flow field regimes, namely, steady flow and alternate attachment regimes, are observed for different L/D and Re values. Depending on the evolution of the near-field flow structures, four different wake patterns, “2S,” “2P,” “2C,” and “aperiodic,” are observed. The corresponding vibration response of the upstream cylinder is characterized as interference galloping and extended vortex-induced vibration. As the L/D ratio increases, the lift enhancement due to flow-induced vibration is seen to be weakened. The detailed correlation between the force generation and the near-wake interactions is investigated. The present findings will augment our understanding of vibration reduction or flow-induced energy harvesting of tandem cylindrical structures.

© 2024 Author(s). All article content, except where otherwise noted, is licensed under a Creative Commons Attribution-NonCommercial-NoDerivs 4.0 International (CC BY-NC-ND) license (<https://creativecommons.org/licenses/by-nc-nd/4.0/>). <https://doi.org/10.1063/5.0207136>

I. INTRODUCTION

Slender cylindrical structures are commonly used in various engineering applications, such as cables of suspension bridges, pipelines of offshore wells, electric lines, masts, and chimneys, among others. Flow-induced vibration (FIV) of such bluff-body-shaped engineering structures is ubiquitous and has received extensive attention in recent decades.^{1–3} The separation and rolling up of shear layers give way to vortex shedding behind cylinders, which in turn causes the pulsating forces on them, thereby inducing FIV.^{4,5} When the vortex shedding frequency is close to the structural natural frequency, synchronization takes place, giving rise to high-amplitude vibrations in the lock-in regime. This phenomenon is called vortex-induced vibration (VIV).⁶ Galloping is another kind of aeroelastic instability, where the resulting self-sustained response amplitude increases with increasing reduced velocity, U_r . Galloping usually occurs on structures with sharp edges as

they are prone to aeroelastic instabilities. Interestingly, adding additional surface protrusions to the surface of a circular cylinder can also give rise to galloping.^{7,8} Furthermore, in tandem arrangement with a considerably small spacing ratio, the downstream cylinder (DC) can induce interference galloping in the response of the upstream cylinder (UC).⁹

In the presence of multiple cylinders, the FIV characteristics get significantly altered compared to the case of a single cylinder due to their mutual interference. An elastically mounted cylinder is likely to exhibit wake galloping due to the strong disturbance coming from the wake of another cylinder placed in the near-field.¹⁰ Previous studies have investigated the amplitude and frequency characteristics of the response, different flow field regimes, vortex shedding patterns, and aerodynamic force generation of the wake galloping phenomenon.^{11–14} Ping *et al.*¹⁵ reported that the lower response branch of

rigidly connected tandem cylinders is quasi-periodic and that it can be divided into two different sub-branches due to frequency detuning. Zhu and Wang¹⁶ numerically studied the effect of an UC and spacing ratio on the motion of a DC. The authors reported that the wake pattern changed significantly with varying spacing ratios and reduced velocities. The downstream circular cylinder exhibited an aperiodic response due to unstable vortex evolution generated by the rectangular and triangular cylinders. Qin *et al.*¹⁷ investigated the FIV of different-sized tandem cylinders, in which the small UC was fixed and the large DC was elastically supported, showing that both vortex shedding and gap shear layer switching could lead to a rapid increase in vibration during the initial transition. Hu *et al.*¹⁸ reported the vibration response of a circular cylinder in the wake of a UC; three vibration responses of the DC, namely, pure vortex resonance, separated pure vortex resonance and wake-induced galloping, and combined pure vortex resonance and wake-induced galloping, were observed. Unlike the vortex shedding vibration mechanism for a single cylinder, there exist other vibration excitation mechanisms in tandem cylinders. Borazjani and Sotiropoulos¹⁹ conducted a study on elastically supported cylinders arranged in series, and they highlighted the significant role of gap flow in initiating and sustaining vibrations in the UC. The gap flow generated substantial oscillatory forces, resulting in the cylinder maintaining large-amplitude and low-frequency oscillations.

Adding more cylinders increases complexity in the flow field, including alterations in the shear layer within the gaps and the merging of vortices in the flow field. Consequently, the FIV behavior of the cylinders also varies. Zhu *et al.*²⁰ studied the fluid force characteristics of three tandem cylinders and pointed out that the fluid forces of the DC are reduced during the transition from continuous reattachment–alternate reattachment to quasi-co-shedding. Tu *et al.*²¹ numerically studied the FIV characteristics of three cylinders in series by varying Re , U_r , and the shear ratio and showed that the FIV response of the middle cylinder and DC is more sensitive to the parameters mentioned above. When the spacing ratio is 5.5, the interference of the DC on the UC is reduced, and the vibration of the UC closely resembles that of a single cylinder. Duong *et al.*²² numerically investigated the wake flow regime of three elliptical cylinders in series and showed that two kinds of vortex shedding frequencies appear in the middle cylinder and DC while the flow regime is quasi-co-shedding (the vortices behind the DC primarily occur due to vortex shedding from the UC) and co-shedding (vortex shedding takes place simultaneously behind three cylinders). Hosseini *et al.*²³ investigated the FIV of six elastically supported cylinders with equal spacing. At a spacing ratio of 3, the flow becomes disordered as the reduced velocity increases. The vibration of the primary cylinder closely resembles that of a single cylinder, while the vibration of the other cylinders exhibits random variations with reduced velocity.

Previous studies have primarily concentrated on assessing the impact of a series of elastically supported cylinders or the wake-induced vibration of the DC. The influence of DC on the FIV of UC has received the least attention. However, it has been shown by a few studies that a DC can give rise to nonlinear and divergent self-excited vibration similar to galloping cylinder response of the UC.²⁴ Zhu and Wang¹⁶ investigated the effect of a C-shaped DC on the vibration feature of UCs. The results show that at $Re = 100$ and spacing of 1.5 D , the UC exhibits the extended body feature; the lift coefficient and amplitude of the UC are reduced by 85.5% and 94.5%, respectively,

due to the interference of the C-shaped cylinder. Zhang *et al.*²⁵ studied the energy harvesting performance of FIV of tandem cylinders with a gap ratio between 0.3 and 3, in which the DC is fixed and the UC is elastically supported. The experimental results show that the resonance region of the UC is broadened by setting the interference cylinder. In addition, Zhang *et al.*²⁶ experimentally investigated the effect of the spacing and shapes of the fixed DC on the FIV of UCs. The gap ratio ranged from 0.15 to 4.5. It is pointed out that when the DC is a square, the synchronous region is increased by 380% compared with that of a single cylinder. However, these studies did not conduct an in-depth analysis of the underlying reason why the presence of the fixed downstream interference cylinder could enhance the vibration of the UC at a low spacing ratio, which will be taken up in this paper.

Summarizing the previous works, many researchers have concentrated on the FIV of the DC in the wake flow. Although a few studies have demonstrated the effect of fixed DC on the UC, the underlying flow mechanisms behind the transition from VIV to galloping of the UC are yet to be clearly understood. Therefore, it is necessary to conduct a systematic, in-depth study to understand the interference mechanism of a fixed DC, especially when the intermediate spacing is small. This is taken up in the present study. Note that the present 2D simulations are carried out in the low Re regime to avoid the effect of three-dimensionality. Due to the relatively low computational cost of 2D simulations, many previous studies also have chosen to study the FIV of bluff-body systems in the low Re regime to capture the essential flow physics and have shown that low Re simulations are of great significance in unraveling the underlying fundamental vortex dynamics behind the FIV of bluff-body-shaped structures. We aim to investigate the following key research questions: (1) What are the wake characteristics for a range of different Re and spacing ratios in the tandem circular cylinder? (2) What are the vibration characteristics and the FIV transition mechanism of the UC for different Re and L/D values? (3) What is the role of wake interference in the intermediate gap between tandem cylinders in changing the hydrodynamic coefficient of the UC? A series of systematic 2D laminar simulations are carried out in this study to address these questions.

The remainder of this paper is organized as follows. Section II comprises of the details of the computational methodology, including the governing equations, the simulation setup, and the verification and validation of the fluid–structure interaction solver. The flow field characteristics of the tandem cylinder system are depicted in Sec. III, while Secs. IV and V present the flow-induced vibration and force generation characteristics of the primary cylinder, respectively. Finally, the salient outcomes of this study are summarized in Sec. VI.

II. COMPUTATIONAL METHODOLOGY

A. Problem definition

The FIV of an upstream elastically supported cylinder with a downstream fixed control cylinder in the low Reynolds number regime is of interest here; see the problem schematic in Fig. 1. The single-degree-of-freedom elastically supported circular cylinder is located upstream and can move freely along the y direction. The fixed control circular cylinder is located downstream. The initial state of the two cylinders is on the same horizontal line. The non-dimensional distance between the centers of the two cylinders, L/D , is systematically varied from 1.25 to 3, where D is the diameter of the circular cylinder.

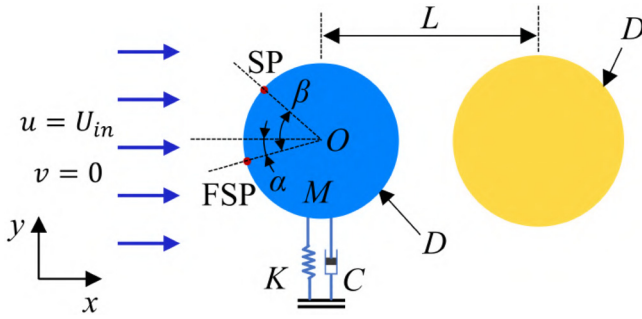


FIG. 1. Schematic of the tandem cylinder system considered in the present study.

To facilitate the analysis in later sections, Fig. 1 shows the front stagnation point of the cylinder marked as FSP and the separation point of the boundary layer marked as SP. The angle α is defined as the angle between the front stagnation point and the center horizontal line of the cylinder. The angle is positive when the front stagnation point is above the center horizontal line of the cylinder and negative when it is below. The angle β is the angle between the separation point of the boundary layer and the front stagnation point.

B. Governing equations

The viscous Newtonian flow is governed by the continuity and unsteady incompressible Navier–Stokes equations as given in the dimensionless form in the following equations:

$$\frac{\partial u_i}{\partial x_i} = 0, \quad (1)$$

$$\frac{\partial u_i}{\partial t} + u_j \frac{\partial u_i}{\partial x_j} = -\frac{\partial p}{\partial x_i} + \frac{1}{Re} \frac{\partial^2 u_i}{\partial x_j \partial x_j}, \quad (2)$$

where $t (= \hat{t} U_{in}/D)$ denotes the dimensionless time, $u_i (= \hat{u}_i/U_{in})$ are the dimensionless velocity components, $x_i (= \hat{x}_i/D)$ are the dimensionless coordinates, $p (= \hat{p}/\rho U_{in}^2)$ is the dimensionless pressure, and $Re (= U_{in}D/\nu)$ is the Reynolds number. Here, D is the diameter of the cylinder, U_{in} is the free-stream velocity, \hat{t} is the dimensional time, \hat{x}_i are the dimensional coordinates, and \hat{u}_i , \hat{p} , ρ , and ν are the dimensional velocity components, pressure, density, and kinematic viscosity of the fluid, respectively. The finite volume method is used to solve the incompressible flow governing equations. The convection terms are discretized in a second-order upwind scheme, and the pressure and velocity coupling are solved by the SIMPLE algorithm. It is known that for a single cylinder subjected to uniform flow, vortex shedding occurs when $Re > 40$ and the wake becomes three-dimensional when $Re \sim 200$.²⁷ Hence, the present study is focused on the low Re regime, where Re ranges from 50 to 170.

The structural system consists of a fixed DC and an elastically supported UC with a single degree of freedom (SDOF) along the cross-flow direction. A typical mass–spring–damper dynamic model describes the motion characteristics of the elastically supported circular cylinder. The motion of the UC in the “y” direction is governed by a second-order linear differential equation describing the dynamics of a SDOF system as follows:

$$M\ddot{\zeta} + C\dot{\zeta} + K\zeta = F_y, \quad (3)$$

where M represents the structural mass, K represents the system stiffness, and $\sqrt{K/M} = \omega_n = 2\pi f_n$, where f_n is the structural natural frequency. ζ is the displacement of the UC, and F_y denotes the lift force along the y direction acting on the cylinder. Equation (3) can be non-dimensionalized using the diameter D and the free-stream velocity U_{in} as the length and velocity scales, respectively, as follows:

$$\ddot{Y} + \frac{4\pi\zeta}{U_r} \dot{Y} + \frac{4\pi^2}{U_r^2} Y = \frac{C_L}{2m^*}, \quad (4)$$

where the non-dimensional displacement $Y = \zeta/D$, damping ratio $\zeta = C/2\sqrt{MK}$, reduced velocity $U_r = \frac{U_{in}}{f_n D} = \frac{Re\nu}{f_n D^2}$, and mass ratio $m^* = M/\rho D^2$. Here, C is the structural damping coefficient, K is the structural stiffness, M is the structural mass of the cylinder per unit length, and f_n is the structural natural frequency. In this study, U_r is proportional to Re as the natural frequency of the structure f_n , kinematic viscosity of the fluid ν , and the cylinder diameter D are kept constant throughout the study. The m^* and ζ of the oscillating cylinder system are considered to be 1.113 and 0.01, respectively, following Zhou *et al.*²⁸ The structural governing equation is numerically solved using the fourth-order Runge–Kutta method.

The two-way coupled fluid–structure interaction (FSI) simulations are carried out using the CFD software Ansys Fluent based on the fully implicit algorithm, where the structural equations are incorporated through user-defined functions. To calculate the two-way coupled response of the UC, the N-S equations are coupled with the structural governing equations in a staggered manner. The second-order accurate spatial and temporal discretization schemes are used in this study with the absolute and relative tolerance criteria kept at 10^{-6} .

C. Verification and validation

The entire computational domain is rectangular with a size of $70D \times 2H$, where D is the diameter of the circular cylinder and H is half of the width of the flow field. In the flow direction, the distance between the center point of the elastically supported cylinder and the inlet is $20D$, while the distance is $50D$ from the center of the elastically supported cylinder to the outlet. The boundary conditions are shown in Fig. 2. The boundary settings of the computational domain include the velocity inlet with $u = U_{in}$ and $v = 0$, the pressure outlet with $du/dx = 0$ and $dv/dx = 0$, and the symmetric upper and lower walls with $du/dy = 0$, $v = 0$.

To avoid the numerical instability caused by excessive mesh deformation due to large displacements of the upstream elastically supported cylinder, the overset meshing strategy is used in the present study. The computational mesh is shown in Fig. 3, which consists of a background mesh and two overset meshes. The partial mesh of the tandem cylinder is shown in Fig. 3(a), and Fig. 3(b) shows an enlarged view of the cylindrical boundary grid. The boundary of the overset mesh domain is $3D$, as seen in Fig. 3(c). To accurately capture the flow field structures, the perimeter of the cylinder is discretized at equal intervals, and the thickness of the first layer grid around the cylinder structure and the mesh growth ratio in the radial direction are $0.001D$ and $1.02D$, respectively. Additionally, the same grid density is used for both overset grid domains.

The effect of domain size on the results is checked by varying the cross-flow height H (20, 25, and $28D$) at $L/D = 3$ and $Re = 100$.

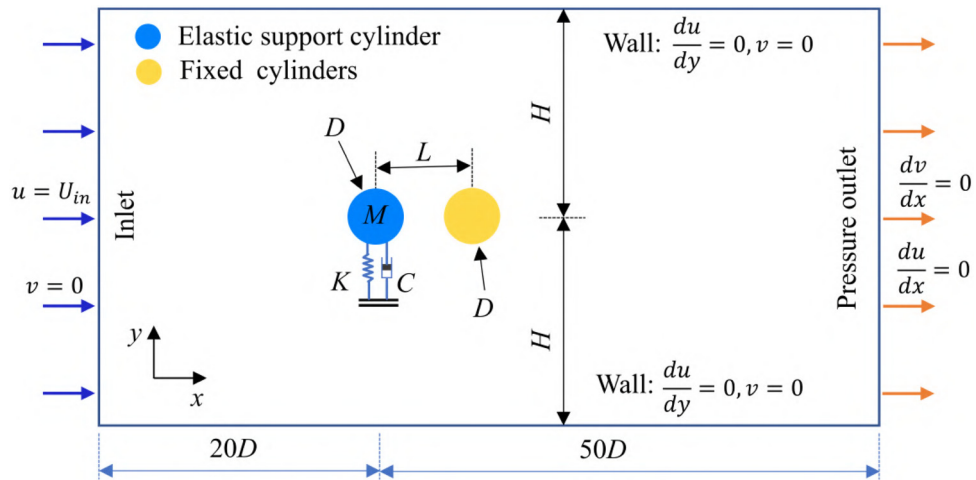


FIG. 2. Schematic of the present computational domain and imposed boundary conditions.

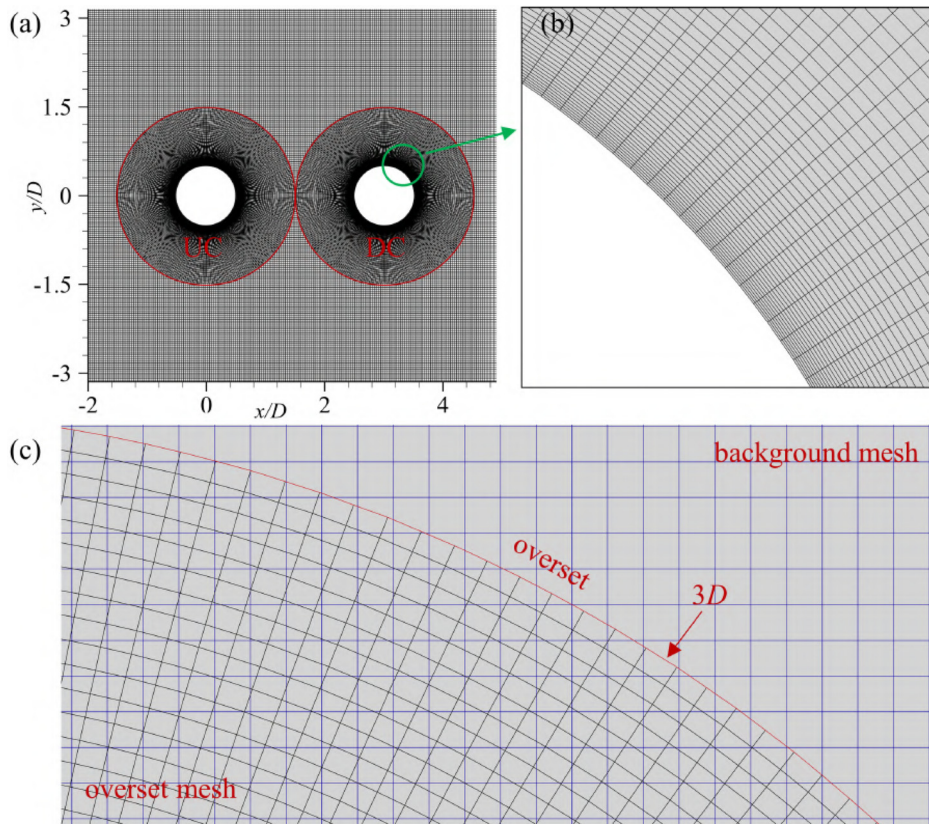


FIG. 3. Computational mesh: (a) the mesh around the tandem cylinder at its initial position; (b) zoomed inset of the mesh near the cylinder; (c) the overset meshing strategy.

The same foreground mesh for the cylinder walls and the same grid size growth rate are used in these three cases. The time step in the domain-independence study is set to 0.008, meeting the requirement of the maximum Courant number to be less than unity to ensure

stability of the solution scheme. The simulation results are shown in Table I, the maximum difference is less than 1%. To reduce the computational cost, the H value of $20D$ is considered by comparing the results of Y_{max} , C_{Dmean} , and C_{Lrms} for these three cases.

08 October 2024 10:08:41

TABLE I. Comparison of results under different heights of the computational domain for $L/D = 3, Re = 100$.

H/D	Background elements	Overset elements	Δt	Y_{\max}	$C_{D\text{mean}}$	$C_{L\text{rms}}$
20	80 896	49 128	0.008	0.595 [...]	1.7309 [...]	0.1796 [...]
25	98 784	49 128	0.008	0.596 [0.17%]	1.7353 [0.25%]	0.1799 [0.17%]
28	102 144	49 128	0.008	0.596 [0.00%]	1.7418 [0.37%]	0.1799 [0.00%]

TABLE II. Results of mesh independence test for flow around two tandem circular cylinders with $L/D = 3$, and $Re = 100$ (considering $H/D = 20$).

Case	Background elements	Overset elements	Δt	Y_{\max}	$C_{D\text{mean}}$	$C_{L\text{rms}}$
Case 1	80 896	42 008	0.003	0.594 [...]	1.7492 [...]	0.1784 [...]
Case 2	92 736	49 128	0.003	0.593 [0.17%]	1.7499 [0.04%]	0.1792 [0.45%]
Case 3	106 029	56 248	0.003	0.593 [0.00%]	1.7513 [0.08%]	0.1794 [0.11%]
Case 4	92 736	49 128	0.001	0.592 [0.17%]	1.7516 [0.10%]	0.1791 [0.06%]

Next, the mesh size and time step independence studies are carried out, keeping the computational domain fixed at $70D \times 40D$ when $L/D = 3$ and $Re = 100$. Cases 1, 2, and 3 are used to check for the grid convergence; and cases 2 and 4, with case 2 being the reference case, are used for non-dimensional time step study. The comparison of vibration response results is presented in Table II. The number of mesh elements of the three groups is gradually increased. Comparing cases 2 and 1, the differences in the maximum dimensionless amplitude Y_{\max} , the mean value of the drag coefficient $C_{D\text{mean}}$, and the root mean square of the lift coefficient $C_{L\text{rms}}$ are found to be 0.17%, 0.04%, and 0.45%, respectively. When the number of elements is further increased to achieve case 3, the differences are reduced to 0%, 0.08%, and 0.11%, respectively. In the time step independence results, the difference is less than 0.2%. Based on these results, the case 2 mesh with a non-dimensional time step of 0.003 is selected for further simulations in this paper.

With the chosen simulation setup, the results of the VIV of a single cylinder obtained using the present fluid–structure interaction solver are compared with the reference results of Bao *et al.*²⁹ in the similar Re regime to check its efficacy. Using the same parameters as Bao *et al.*,²⁹ a comparison of the dimensionless displacement of the cylinder is shown in Fig. 4. It can be seen that the present results are in good agreement with the reference results. Hence, the present solver can be used for the low Re regime with confidence.

III. FLOW FIELD CHARACTERISTICS

In order to understand the effect of a downstream control cylinder, we systematically study the FIV characteristics of the primary cylinder and the underlying wake dynamics for a range of Re and L/D values. We first characterize the wake patterns through a detailed regime map and unravel the vortex interactions that underline the manifestation of different variety of wake patterns.

A. Characterization of different wake regimes

Different wake regimes are characterized by varying the Re and L/D values, and the wake regime map is presented in Fig. 5. The wake can be broadly distinguished into two different regimes according to the development of the shear layer:³⁰ the steady flow regime (denoted

by I, where there is no vortex shedding behind the DC) and the alternating attachment regime (denoted by II). As the L/D value increases from 1.25 to 3, the range of Re where steady flow occurs gradually decreases from $Re \leq 80$ to $Re \leq 60$, and no vortex shedding occurs in this region. On the other hand, the alternating attachment regime is predominant for $Re \geq 70$. The wake patterns are further classified according to the vortex shedding pattern of the two cylinders. As shown in Fig. 5, the alternating attachment regime can be divided into four sub-regions: (i) “2S” (two single isolated vortices are shed in an oscillation cycle of the cylinder), (ii) “2C” (two counter-rotating vortex pairs are shed in an oscillation cycle of the cylinder), (iii) “2P” (two co-rotating vortex pairs are shed in an oscillation cycle of the cylinder),³¹ and (iv) the “aperiodic” wake regime (vortex shedding takes place completely irregularly with no periodicity), respectively. It can be seen from the flow regime classification diagram that the characteristics of

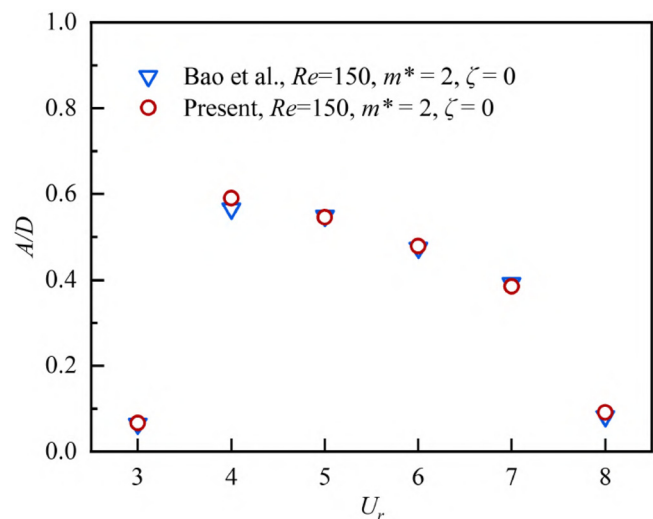


FIG. 4. Validation of the fluid–structure interaction solver for the VIV of a single circular cylinder; here, A/D is the non-dimensional amplitude of the vibration response.

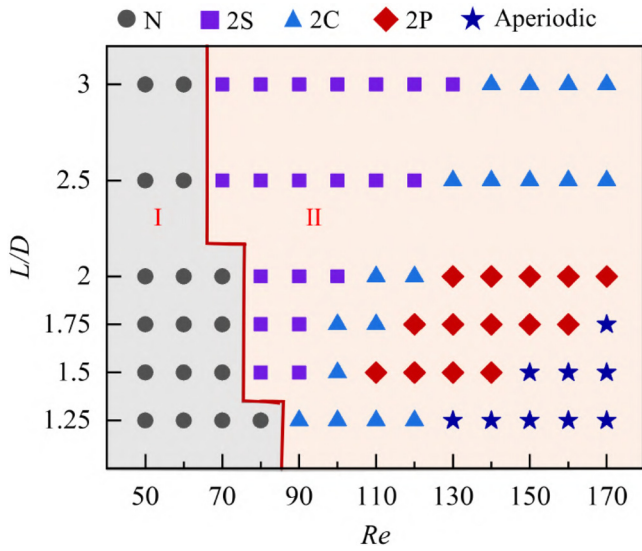


FIG. 5. The wake regime map in Re - L/D parametric space, where I represents the regime without vortex shedding, II represents the regime of alternate reattachment; the classification of wake based on the vortex shedding patterns: “N” (no vortex shedding), “2S,” “2C,” “2P,” and “aperiodic.”

the flow field are sensitive to Re and L/D . A detailed analysis of the flow field interactions is presented in Sec. III B.

B. Underlying vortex interactions

The wake patterns for the steady flow regime and the 2S vortex shedding pattern in the alternate reattachment regime are shown in Figs. 6 and 7, respectively. The vorticity is non-dimensionalized, considering U_{in} as the reference velocity scale and D as the reference length scale, as $\omega_z^* = \omega_z D / U_{in}$. In the steady flow regime (at $L/D = 1.75$ and $Re = 60$), the shear layer, separating from the UC, directly crosses over the DC, and no vortex shedding takes place behind the DC; see Fig. 6. The displacement (Y) and lift coefficient (C_L) of the UC are practically zero in this regime. Figure 7 shows the temporal evolution of the flow structures around the cylinders, the pressure coefficient (C_p) around the cylinders, and the corresponding time histories of the C_L and Y (at $L/D = 1.75$ and $Re = 80$). Here, the clockwise vortices are marked in blue (negative), while the counter-clockwise vortices are marked in red (positive). The resulting wake pattern is characterized as a typical Kármán vortex street.

At 1#, the vortex P1 is seen to be separated from the shear layer of the DC, while the positive shear layer P2 generated by UC remains completely attached to the lower surface of DC. The negative vortex above the DC N1 is shed alternatively, and the negative shear layer N2 in the gap begins to roll up, adhering to the DC. As a result, the

pressure on the upper surface of UC is lower than that on the lower surface, and the pressure difference of the DC is opposite to that of UC at this moment. At 2#, as the UC reaches the maximum positive displacement, the negative shear layer in the gap starts adhering to the upper surface of DC. The shear layer P2 rolls up and squeezes the vortex N1. The pressure on the upper surface of UC increases significantly. At 3#, the vortex N1 is separated, and the remaining shear layer merges with the negative shear layer N2, forming a new shear layer labeled N2*. The negative pressure areas of UC and DC are seen to get reversed compared to those at instance 1#. The vortex shedding process at instances 3# to 5# is the same as that at instances 1# to 3#, but the vortex shedding direction is the opposite. In Fig. 7(a), the C_L and the Y time histories follow the same trend. Within the 2S pattern sub-region, there is a distinctive wake pattern characterized by two-layered vortex streets, as shown in Fig. 7(b). This phenomenon is more pronounced at lower Re and $L/D \geq 2$.

As shown in Fig. 5, the 2P and 2C vortex shedding patterns occur in a wide range of Re and L/D . Figures 8 and 9 show the evolution process of 2P and 2C vortex shedding patterns and the C_p around the cylinders for different Re and L/D values, respectively. In Fig. 8, the cylinders are situated at the middle position at 1#. The remaining shear layer from the negative shedding vortex of the previous cycle is marked as N1, while the negative shear layer within the gap is labeled as N2. Below the tandem cylinder, the positive shear layer from the UC has merged completely with that of the DC and is marked as P2. Both UC and DC have small pressure on the upper surface and high pressure on the lower surface. At 2#, the UC reaches the positive maximum displacement. The downward-curling vortex N1 squeezes the shear layer P2, separating it from DC. On the upper surface of the DC, the shear layer N2 is fully attached to the DC, while the shear layers N1 and N2 remain separate. Conversely, the shear layer N2 promotes the shear layer N1 to separate from DC. At 3#, the UC returns to the middle position. The shear layer P2 detaches from the DC due to the pushing and truncation effect of the shear layer N2 and P3, the shear layer N1 also sheds from DC. During the half cycle (from 3# to 5#) with negative motion displacement, the vortices N2 and P3 shed from the DC in a similar manner. In the downstream far-field of the DC, the vortices with the same direction between the two periods merge. The interference effect of DC results in a noticeable harmonic component of the frequency spectra of C_L , with the two peaks being almost equal.

Figure 9 illustrates the evolution process of the 2C vortex shedding pattern. This vortex shedding pattern is observed between the 2S and the 2P or aperiodic wake regimes (when $L/D \leq 2$) and on the right side of the 2S pattern (when $L/D > 2$). At 1#, the positive shear layers P1 + F1 below DC are connected, and there are two shear layers, named E1 and N1, above DC and in the gap. At 2#, the shear layer N1 attaches to the upper surface of DC and combines with E1 to form the new vortex named N1 + E1. At time 3#, vortex P1 + F1 shedding from the DC is found to occur. Compared with shear layer

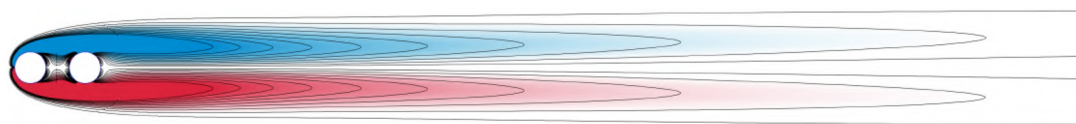


FIG. 6. The steady wake pattern ($-1 \leq \omega_z^* \leq 1$) at $L/D = 1.75$, $Re = 60$.

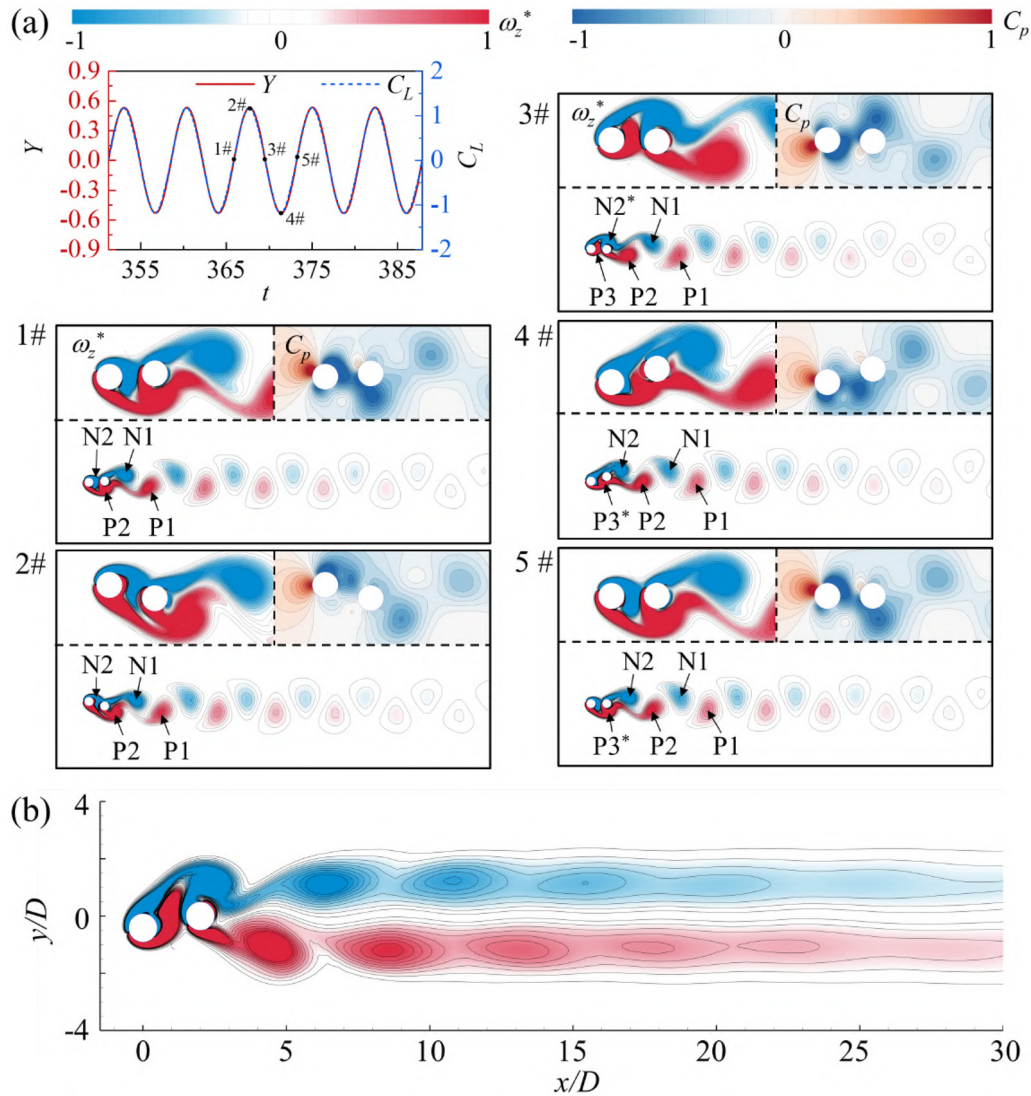


FIG. 7. The “2S” vortex shedding pattern ($-1 \leq \omega_z^* \leq 1$) at (a) $L/D = 1.75, Re = 80$; and (b) $L/D = 2, Re = 80$ and the corresponding time histories Y and C_L of the UC.

P3 at 3# in Fig. 8, the truncation effect of the remaining shear layer F2 is weakened, and the combination of N1+E1 is not destroyed, but they shed together from the DC at 5# in the negative half cycle. In the downstream far-field of the DC, two vortices with the same direction merge completely into a vortex, the same as the typical Kármán vortex street. The evolution process of the 2S, 2C, and 2P patterns reveals that with increasing Re , the vortex shedding pattern gradually transitions from the 2S pattern to the 2P pattern, while the downstream far-field will evolve to the typical Kármán vortex street.

At small L/D and high Re , the wake behind the tandem cylinders is characterized by an aperiodic vortex shedding pattern (aperiodic pattern), represented by a five-pointed star in the sub-region of Fig. 5. The corresponding time histories of C_L and Y of the UC, the C_p around the cylinders, and the evolution process of vortex shedding are

shown in Fig. 10. It can be noted that the shedding pattern around the UC and the displacement of the UC are mostly periodic. However, the interference of the gap flow and, in turn, the wake downstream become aperiodic. At 1#, vortices N1 and P1 are formed behind the DC. At 2#, as the UC reaches its maximum positive displacement, the negative shear layer N2 is attached to the upper surface of the DC. The positive shear layer below the UC is truncated by the DC, forming parts P2 and P3. Simultaneously, vortices N1 and P1 shed from the DC. At 3#, shear layer P3 cuts vortex N2 into two parts, forming shear layers N3 and N4 at 4#. It can be seen that at 4#, the shear layer P3 has attached to the lower surface of the DC, and the vortex P2 begins to separate from the DC. At 5#, the vortex P3 is divided into two parts by the shear layer N4. A new vortex labeled N3* emerges due to the merging of N2 and N3. At 6#, the shear layer N4 attaches to the upper surface of the DC,

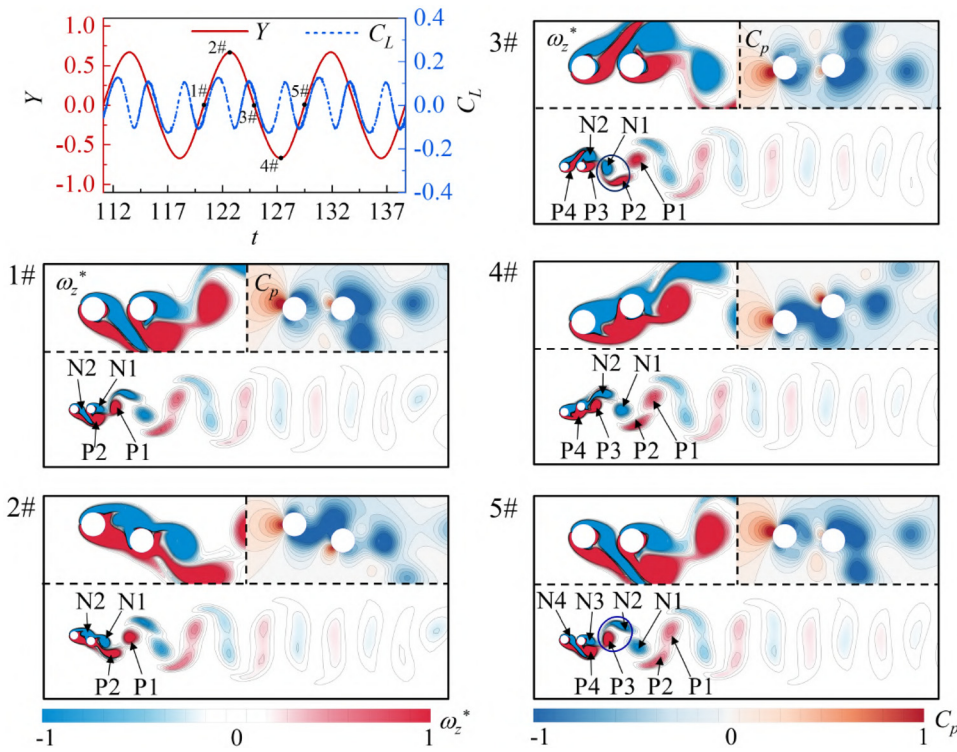


FIG. 8. The “2P” vortex shedding pattern ($L/D = 2, Re = 150$) in the alternate attachment regime and the corresponding time histories Y and C_L of the UC.

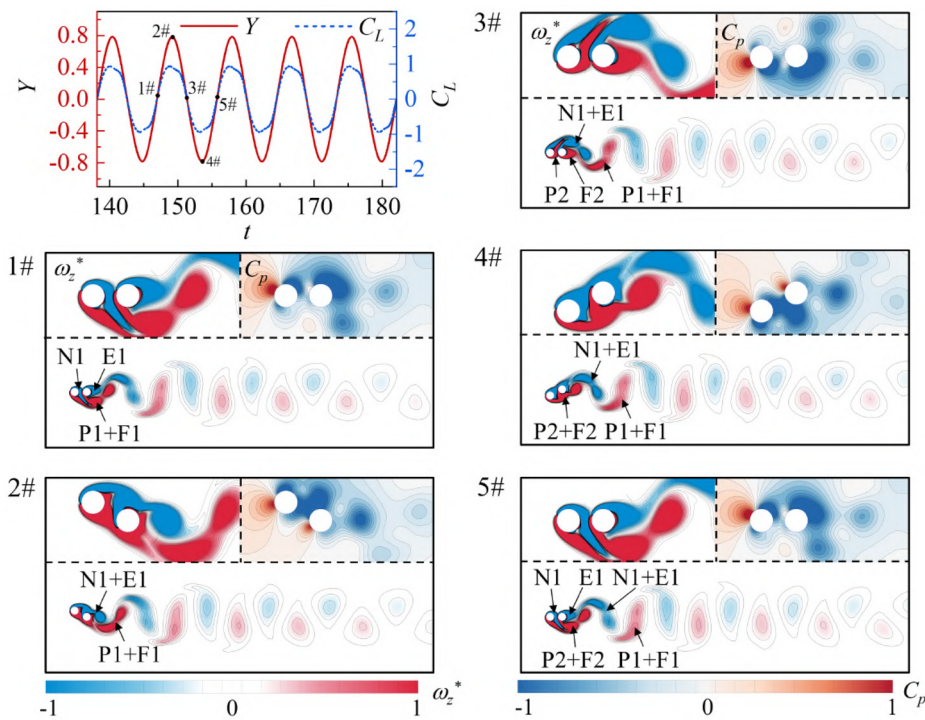


FIG. 9. The “2C” vortex shedding pattern ($L/D = 1.5, Re = 100$) in the alternate attachment regime and the corresponding time histories Y and C_L of the UC.

08 October 2024 10:08:41

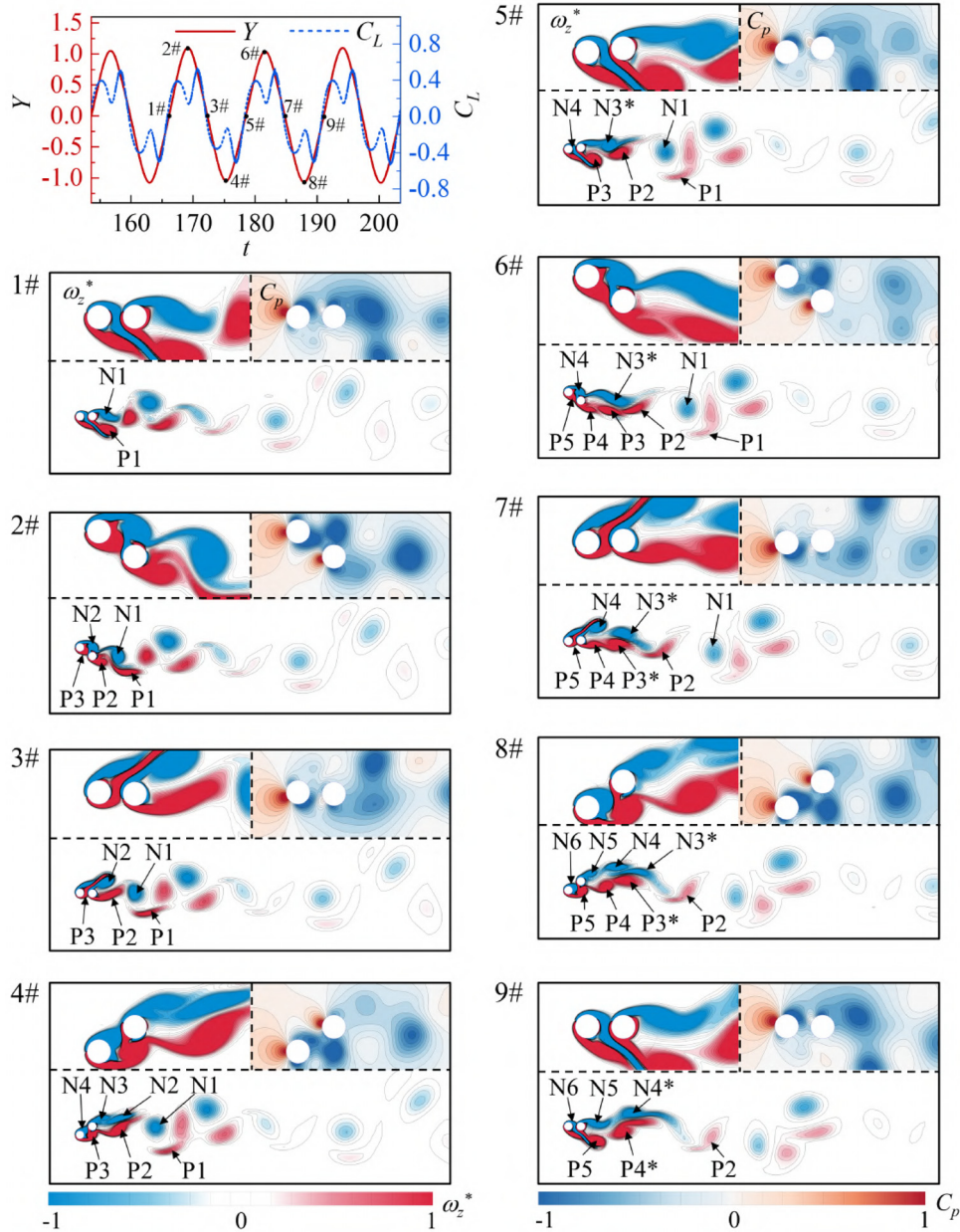


FIG. 10. The “aperiodic” vortex shedding pattern ($L/D = 1.5, Re = 160$) in the alternate attachment regime and the corresponding time histories Y and C_L of the UC.

and $N3^*$ separates from the DC. Below the DC, the vortices $P2, P3,$ and $P4$ form a long, narrow vortex strip. The vortex $P3$ merges with part of $P4$ to form a new vortex, $P3^*$, at $7\#$. The vortex $N4$ is divided into two parts by the shear layer $P5$ at $7\#$ and evolves into vortices $N4, N5,$ and $N6$ at $8\#$. Finally, vortices $N4$ and $N3^*$ also merge to form $N4^*$ at $9\#$, and the same is observed for vortices $P4$ and $P3^*$. The time history, frequency spectra, wavelet spectra of C_L for the DC and the phase portraits of C_L and C_D of the DC at $L/D = 1.5$ and $Re = 160$ are presented in Figs. 11(a)–11(d), respectively. It can be seen that the

time history of C_L is irregular with broadband frequency spectra, indicative of the aperiodic nature of the flow field. It is evident that there is no distinct periodic attractor in the phase space. In comparison to the other three sub-regions in Fig. 5, this sub-region exhibits a complex process of wake vortex shedding and merging, lacking regularity in the vortex shedding process. The instability of the shear layer separated from the UC can be attributed as the primary agency for triggering this aperiodicity over the DC. Hence, we classify this flow regime as an aperiodic wake pattern.

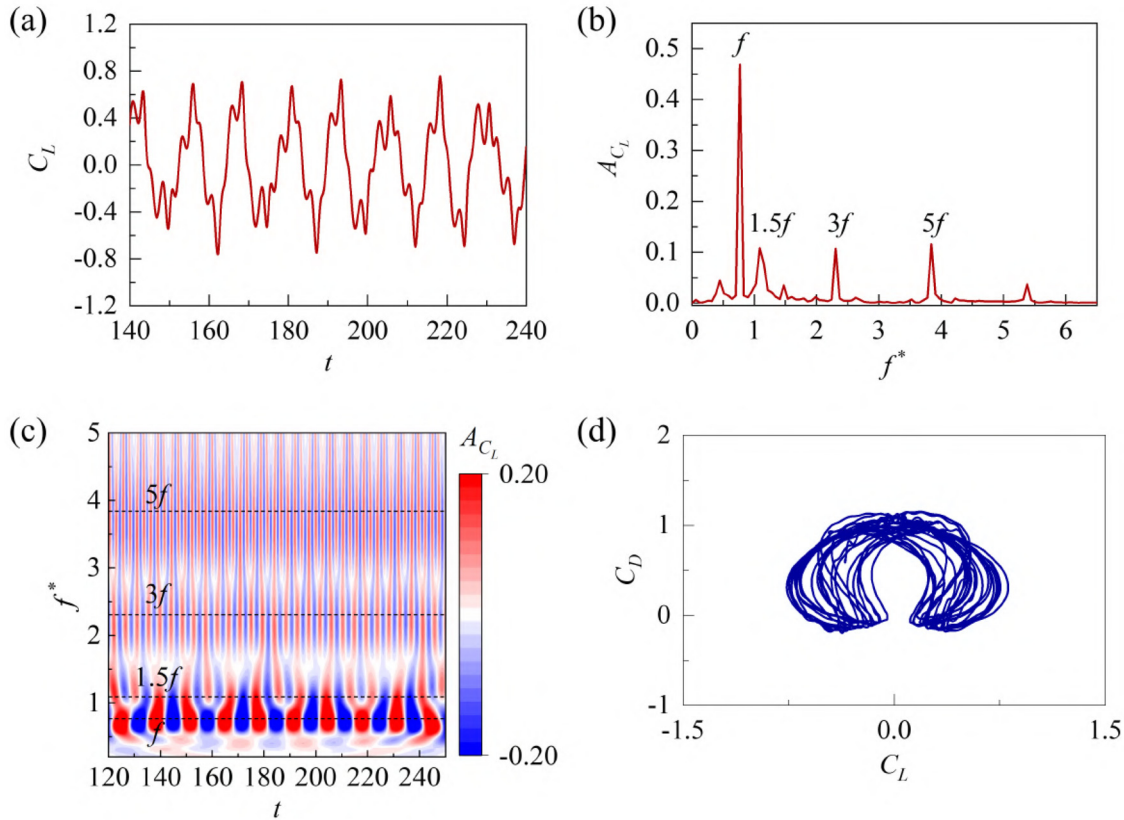


FIG. 11. Time series analysis of C_L of DC for $L/D = 1.5$, $Re = 160$: (a) time history; (b) frequency spectra; (c) wavelet spectra; and (d) $C_L - C_D$ phase portrait.

C. Analysis of wake characteristics

The wake characteristics behind the tandem cylinder system are analyzed in this subsection. When the UC is in the equilibrium position just before the start of the upward movement, the flow field contour is considered to calculate the vortex width at a position of $x/D = 10$ downstream. For the streamwise distance, the center-to-center distance between the two adjacent co-rotating vortex cores is calculated at $x/D = 10$ downstream. All the cases are represented with the same contour levels. It is worth noting that, for the aperiodic cases, the average and standard deviation of the wake width and streamwise distance of the 10 consecutive oscillation cycles are calculated; the results are plotted with the corresponding error bars.

Figure 12(a) illustrates the variation of the near-wake vortex width (L_w/D) for different U_r and Re values. The error bars in $L/D = 1.25, 1.5$, and 1.75 represent the statistical results of the varying L_w/D in the aperiodic pattern region. Two representative cases are presented in Fig. 12(b). At $L/D \leq 2$, except for the aperiodic regime, the wake width gradually increases with increase in the reduced velocity, however, with a decreasing rate of increment. In the aperiodic regime, a variety of shedding patterns appear due to complex vortex shedding and merging; there is a different wake width in the wake flow. Comparing the vortex shedding pattern classification in Fig. 5, the L_w/D value increases rapidly in the 2S and 2C regimes, while only

small changes are observed in the 2P region. For L/D values between 2.5 and 3 and $Re < 110$, the vortex shedding phenomenon exhibits a 2S pattern with a double-layered vortex street, and the variation in L_w/D is small. Subsequently, as the vortex shedding transformed to a 2S pattern with the single-layer vortex street, the L_w/D ratio was found to increase gradually.

Figure 13(a) presents the streamwise distance (L_s/D) for the two adjacent co-rotating near-wake vortices as a function of U_r and Re . Two representative cases are presented in Fig. 13(b). Different L_s/D values are observed in the consecutive vortex shedding periods in the aperiodic wake regime, which can be attributed to the complex vortex shedding behind the DC. When the L/D value ranges from 2.5 to 3, L_s/D increases with increasing U_r , indicating a decrease in the vortex shedding frequency. Based on the vortex shedding pattern classification in Fig. 5, the L_s/D value gradually increases as the vortex shedding pattern evolves from 2S to 2C and 2P. When located in the two-layered vortex street, the change of L_s/D is small.

IV. FLOW-INDUCED VIBRATION CHARACTERISTICS

In the previous section, the different wake regimes observed with different Re are analyzed. The results have shown that a strong interference effect due to the presence of the DC affects the vortex shedding patterns of the UC, in turn significantly altering the associated

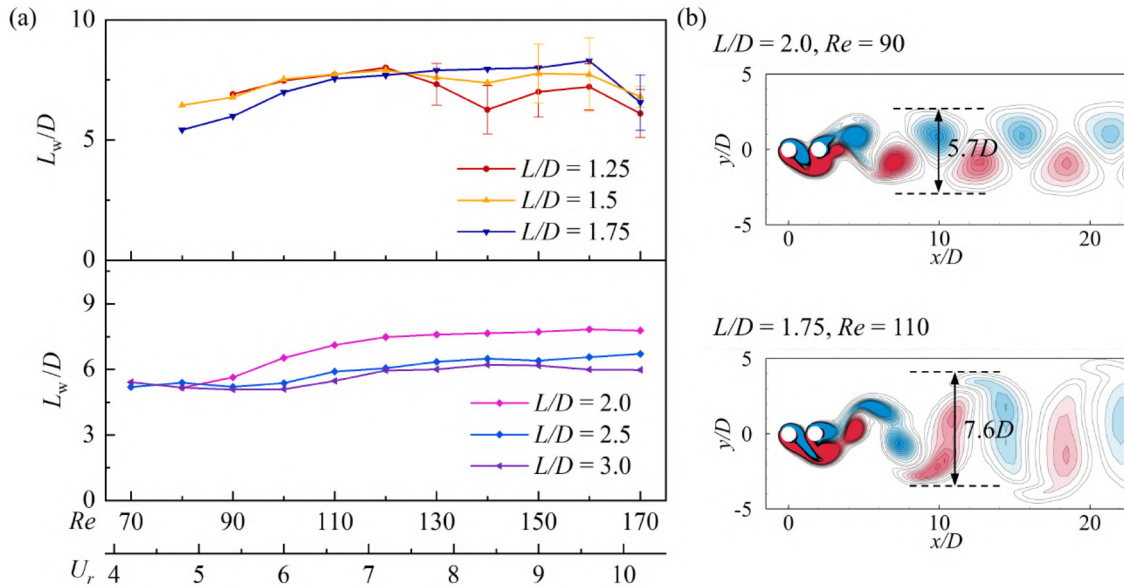


FIG. 12. (a) The variation of wake width at different U_r and Re values and (b) the details of two representative cases of vortex width calculations in the near-wake.

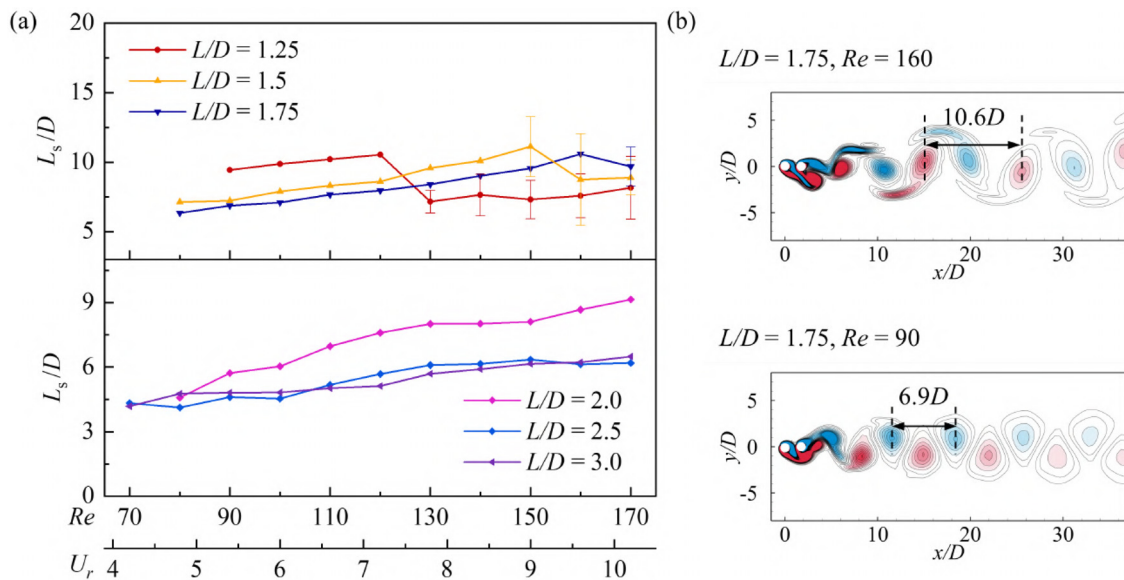


FIG. 13. (a) The variation of vortex spacing at different U_r and Re values and (b) the details of two representative cases of the streamwise vortex spacing calculation in the near-wake.

aerodynamic forces. Next, in this section, the flow-induced vibration characteristics of the UC are presented.

A. Amplitude and frequency characteristics

Figure 14 shows the variation of the dimensionless amplitude (A/D) and the frequency ratio (f_{osc}/f_n) of the flow-induced vibration response of the UC as a function of U_r , in comparison to the results of

a single cylinder and large spacing ratio, $L/D = 15$. Here, the amplitude A is defined as $0.5(y_{max} - y_{min})$, where y_{max} and y_{min} are the maximum and minimum response amplitudes, respectively. Figure 15 presents the dynamical classification of the vibration response, in which I represents the steady flow regime, where the displacement of the UC is close to 0 and II corresponds to the alternating attachment regime. Two vibration types of the UC are distinguished, by color blocks: extended VIV and interference galloping (IG). As can be seen

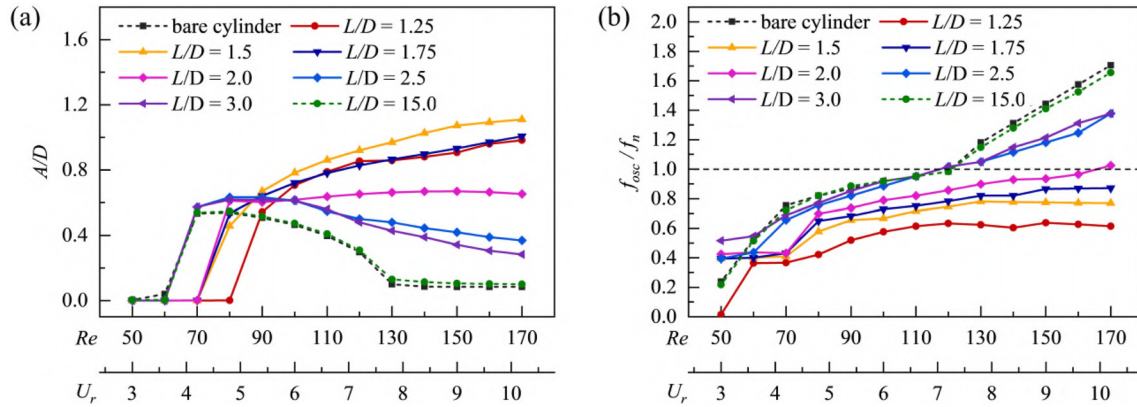


FIG. 14. Variations in (a) the dimensionless amplitude (A/D) of the FIV response of the UC and (b) the corresponding dimensionless frequency ratio (f_{osc}/f_n) with Re .

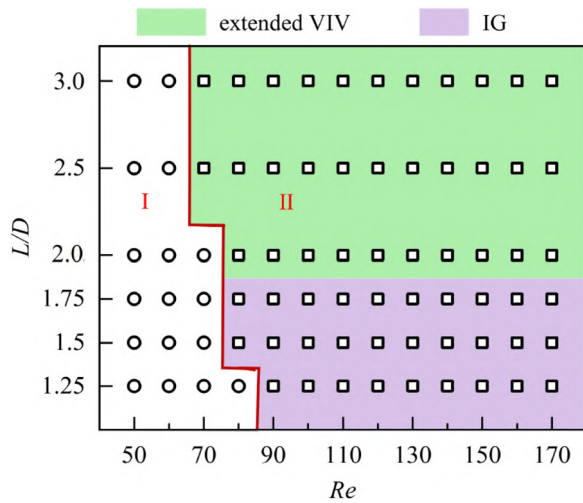


FIG. 15. Dynamical classification of the vibration response, where circle corresponds to region I, square to region II.

in Fig. 14(a), the dimensionless amplitude of the UC increases gradually with increasing U_r and has a similar trend when L/D varies between 1.25 and 1.75. In addition, the amplitude is the largest when $L/D = 1.5$. When $L/D \geq 2.5$ and $U_r \geq 5.4$, the dimensionless amplitude shows a decreasing trend with increasing L/D ; the amplitude does not change significantly for $L/D = 2$. It can be seen from Fig. 14(b) that the dimensionless frequency of the UC gradually increases with increasing U_r after the UC starts vibrating. In addition, the dimensionless frequency also increases with increasing L/D .

When L/D is 1.25, 1.5, and 1.75, the dimensionless frequencies are locked-in at 0.62, 0.77, and 0.87, respectively, and the vibration response of the UC can be characterized as the interference galloping.³² The interference effect of the DC on the vibration of the UC gradually weakens with increasing L/D . When L/D is greater than a critical threshold, the response of the UC transitions to pure VIV.³³ As can be seen from Figs. 14(a) and 14(b), when $L/D = 15$, the dimensionless amplitude and the frequency ratio of the UC response are

completely consistent with that of a single circular cylinder. In Fig. 14(a), when L/D is between 2.5 and 3, the dimensionless amplitude reaches its maximum at $U_r = 4.8$ and then gradually decreases with increasing U_r . It is worth noting that, when $U_r \geq 7.8$, the dimensionless displacement of the UC is larger than that of a single cylinder. The dimensionless frequency of the UC increases from 0.68 to 1.37 when L/D is between 2.5 and 3. When $L/D = 2$, the maximum frequency ratio is 1.02 at $U_r = 10.2$, which is smaller than that observed when the L/D value lies between 2.5 and 3. This indicates that due to the interference effect of the DC, there is a wider lock-in region when $L/D = 2$. According to Chen *et al.*,³⁴ when L/D falls between 2 and 3, it can be classified as extended VIV. The range of L/D also aligns with that reported by Bokaian and Geoola.³⁵

According to the classification results of the wake regime presented in Fig. 15, there is no vortex shedding behind the cylinder in the steady flow regime, and the displacement of the UC is close to zero in this regime. As U_r increases, the wake changes from the steady flow to the alternate attachment regime, and the UC begins to vibrate with a large amplitude. Comparing with the classification in Fig. 5, the wake shifts from steady flow to the 2S, and then evolves into 2C, 2P, and aperiodic pattern with increasing U_r at $L/D = 1.5$, which is different from the evolution process from 2C to aperiodic pattern at $L/D = 1.25$, resulting in a small starting velocity and larger vibration amplitude of the former. At $L/D = 1.75$, the larger transition range of the 2P pattern and smaller distribution of the aperiodic pattern result in smaller vibration amplitudes compared with the case when $L/D = 1.5$.

B. Phase difference characteristics

Using the Hilbert transform, the instantaneous phase of the lift coefficient and the dimensionless amplitude are calculated, and then the instantaneous phase difference between the two is obtained. Finally, the root mean square value of the instantaneous phase difference (ϕ_{rms}) is estimated to evaluate the phase characteristics of the lift coefficient and the dimensionless amplitude; see Fig. 16. When $L/D \leq 1.75$, the value of ϕ_{rms} gradually increases with increasing U_r . The ϕ_{rms} increases to 51° when $U_r = 10.2$ and $L/D = 1.75$, and it increases to 110° when L/D increases to 2. Consequently, the increase in the dimensionless displacement decreases with increasing U_r . At $L/D = 2$, the ϕ_{rms} increases significantly, and the enhancing effect of lift

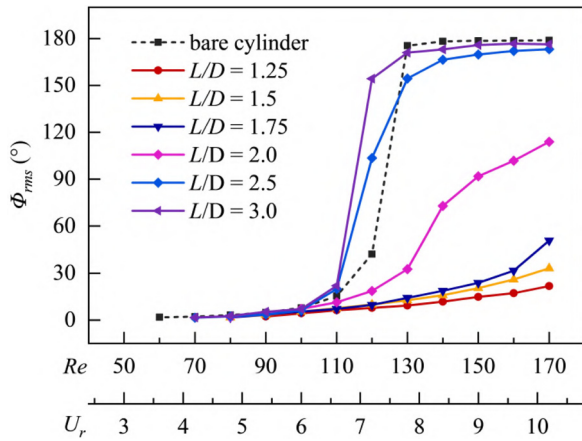


FIG. 16. Variation of the phase difference between lift force and transverse displacement with Re .

on the cylinder vibration weakens, resulting in a small change in the UC amplitude. The ϕ_{rms} value of the UC is similar to that of the single circular cylinder for $L/D \geq 2.5$. When $U_r > 7.8$ and $L/D \geq 2.5$, the ϕ_{rms} reaches 180° (the lift coefficient and the dimensionless displacement are in anti-phase condition), resulting in continuous decrease of the response amplitude of the UC with increasing U_r .

V. FORCE CHARACTERISTICS OF THE UPSTREAM CYLINDER

Figure 17 shows the variation of the root mean square value of the lift coefficient (C_{Lrms}) and the mean value of the drag coefficient (C_{Dmean}) of the UC with increasing Re and U_r . It can be seen from Fig. 17(a) that the C_{Lrms} is almost zero at the steady flow regime due to the absence of vortex shedding. As the U_r increases, the C_{Lrms} undergoes a sudden jump with the change in flow regime. When $L/D = 1.25$ and Re ranges from 80 to 90 or $L/D = 1.5$ and Re ranges from 90 to 100, the change in C_{Lrms} is very small in the alternate attachment regime and then gradually decreases with increasing U_r . On the contrary, the C_{Lrms} of the UC jumps to its maximum along

with the change in flow regime and then decreases with increasing U_r when $L/D \geq 1.75$. It is worth noting that the C_{Lrms} slightly increases when $U_r \geq 7.2$ and $L/D \geq 2.5$ compared to the single cylinder case. This coincides with a slow decreasing trend of the response displacement of the UC. It can be seen from Fig. 17(b) that the C_{Dmean} value for different L/D follows the same trend. There is a small decrease in the steady flow regime. Then, it increases significantly after the onset of the UC vibration and subsequently decreases with increasing Re . The C_{Dmean} of the UC is larger than that of a single cylinder when $U_r > 6.6$. It is worth noting that the critical Re for steady to unsteady flow transition decreases as L/D increases. At $L/D = 15$, the interference effect of the DC on the UC disappears, and the UC and the single circular cylinder are seen to have the same C_{Lrms} and C_{Dmean} .

The time histories and frequency spectra of C_L for $L/D = 2$ and different Re are shown in Fig. 18. It can be seen that the frequency spectra primarily comprise a dominant frequency peak (vortex shedding frequency) and its triple harmonic. Due to the interference effect of the DC on vortex shedding, the triple frequency harmonic component on the time history of C_L becomes more significant as Re increases. Notably, at $Re = 160$, the magnitude of the triple harmonic component exceeds the magnitude of the fundamental frequency and becomes the dominant shedding frequency. Previous studies³⁶ have shown that the triple harmonic lift is related to three vortices shedding behind the cylinder, resulting in a 2T vortex shedding pattern. For the present tandem cylinder system, although the 2T vortex shedding pattern does not appear, the triple harmonic frequency of C_L of UC can be attributed to the shear layer interaction in the intermediate gap flow. Wavelet analysis of the C_L time history is carried out for $Re = 120$ and $Re = 160$ at $L/D = 2$; see Fig. 19. The contour represents the variation of the Continuous Wavelet Transform coefficient with non-dimensional time. The black dotted line is the natural frequency (f_n) of the elastically supported cylindrical structure. From the contour in Fig. 19(a), it can be seen that when $Re = 120$, the peaks A1 and C1 at the positive half period of the lift coefficient are located between the positive and negative peaks of the triple harmonic component. When $Re = 120$, the two peaks are mainly affected by the first-order fundamental component. While $Re = 160$, the variation of the lift coefficient is similar to that of $Re = 120$; see Fig. 19(b). However, the peaks (A2 and C2) of the lift coefficient coincide with the peak of the triple

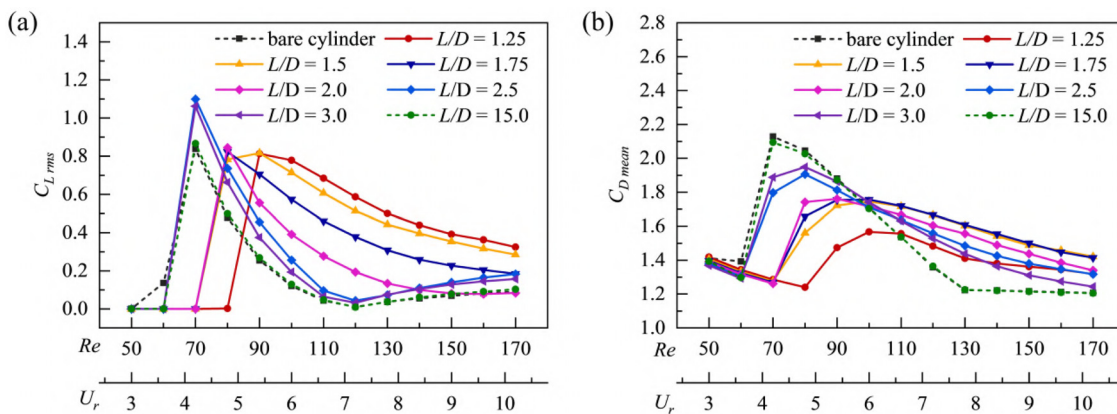


FIG. 17. The variation of (a) C_{Lrms} and (b) C_{Dmean} with Re and U_r for various L/D values.

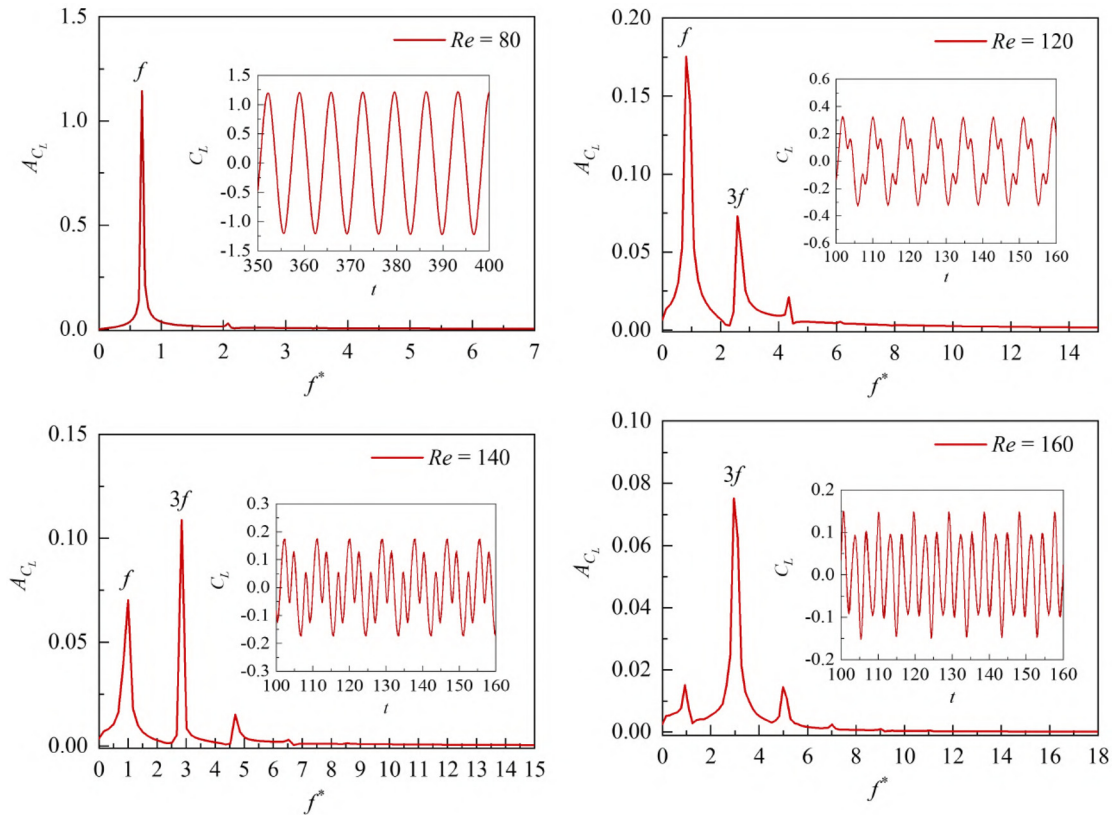


FIG. 18. The time history and frequency spectra of the C_L for $L/D = 2$ and different Re .

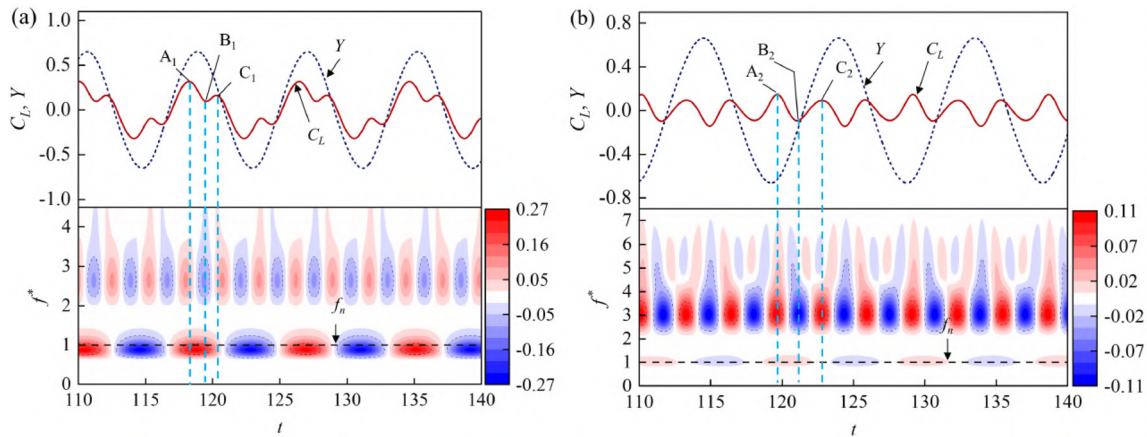


FIG. 19. The continuous wavelet transform (CWT) results of the C_L time histories: (a) $L/D = 2$, $Re = 120$; (b) $L/D = 2$, $Re = 160$.

harmonic component, that is, the lift coefficient is mainly dominated by the triple frequency harmonic lift.

Figures 20–22 show the angle of the separation point of the boundary layer, the variation of the surface pressure coefficient (C_p), the contour of C_p and vorticity at different instances of Y and C_L time

histories for different Re . Figure 20(a) shows the lift coefficient and dimensionless amplitude of the UC. In the C_p contour, the solid and dotted lines represent the velocity $u^* = 0$ and $u^* = 1$, respectively, where $u^* = u/U_{in}$ is the normalized velocity. The separation point of the boundary layer can be determined from $u^* = 0$, while the distance

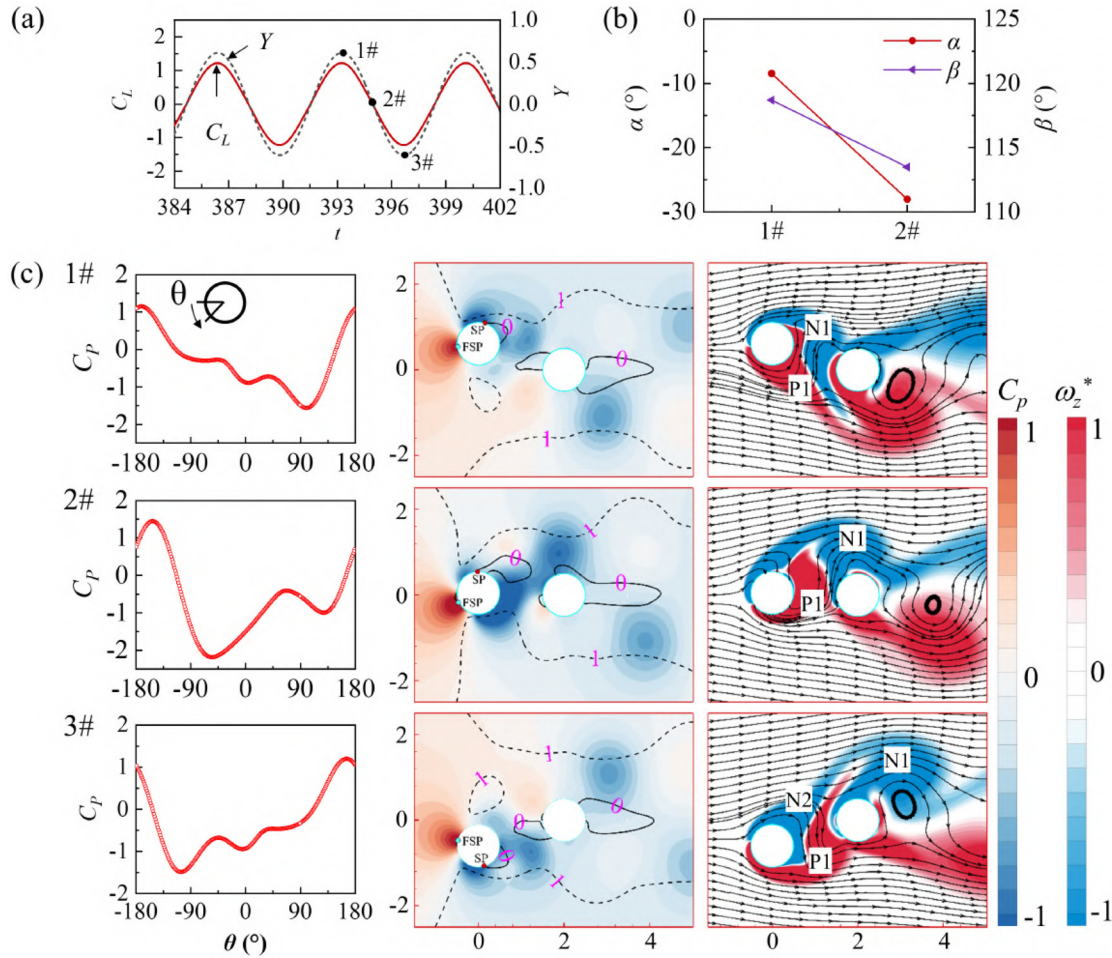


FIG. 20. (a) Lift coefficient and dimensionless amplitude, (b) angle between the front stagnation point and the separation point of the boundary layer at 1#, and (c) the surface pressure coefficient and the contour of the surface pressure coefficient and the local vorticity at different times when $Re = 80$.

between $u^* = 0$ and $u^* = 1$ indicates the thickness of the shear layer. Due to the symmetric motion of the UC, the angles of α and β are only shown from 1# to 2# in Fig. 20(b). In Fig. 20(c), at 1#, the separation point of the boundary layer is located on the upper surface of UC, and the angle β between the separation point of the boundary layer and the front stagnation point is 118.7° (the definition of the angle is provided in Fig. 1). In the vorticity contours, the formation of the clockwise vortex N1 results in the maximum pressure difference between the upper and lower surfaces of the UC and, in turn, the maximum upward lift coefficient at 1#. From the instances of 1# to 2#, the shear layer P1 moves with upward velocity and the intensity gradually increases, a small counterclockwise vortex is formed in the gap. Meanwhile, the clockwise vortex N1 begins to shed, and the supply of the boundary shear layer to the vortex N1 is weakened. The pressure on the upper surface of the UC increases while the pressure on the lower surface decreases, causing the lift coefficient to gradually decrease to zero. From 2# to 3#, the counterclockwise vortex P1 causes a downward velocity in the gap, the pressure on the lower surface of the UC is lower than that on the upper surface, and

the downward lift coefficient gradually increases. There is no harmonic interference effect at this Re .

The harmonic components of C_L emerge as the Re value increases; see Fig. 21(a). It can be seen that the angle β between the separation point of the upper surface boundary layer and the front stagnation point is smaller compared to that observed in $Re = 80$; see Fig. 21(b). In Fig. 21(c), at 1#, the clockwise vortex N1 induces an upward flow velocity in the gap and generates a positive lift force on the UC. At 2#, the upper separation point of the boundary layer moves counterclockwise. The shear layer P1 is displaced to the rear side of the UC, and a small counterclockwise vortex is formed. The overall pressure level on the lower surface reduces, resulting in a decreased lift coefficient. From 2# to 3#, the counterclockwise vortex in the gap moves upward with the water flow, disrupting the connection between vortex N1 and the upper boundary layer of the UC. The separation point of the shear layer P1 moves downward, and the pressure level on the lower surface of UC increases, resulting in a slightly increased lift coefficient. At 4#, the connection between vortex N1 and the UC weakens further, reducing the positive lift coefficient generated by N1

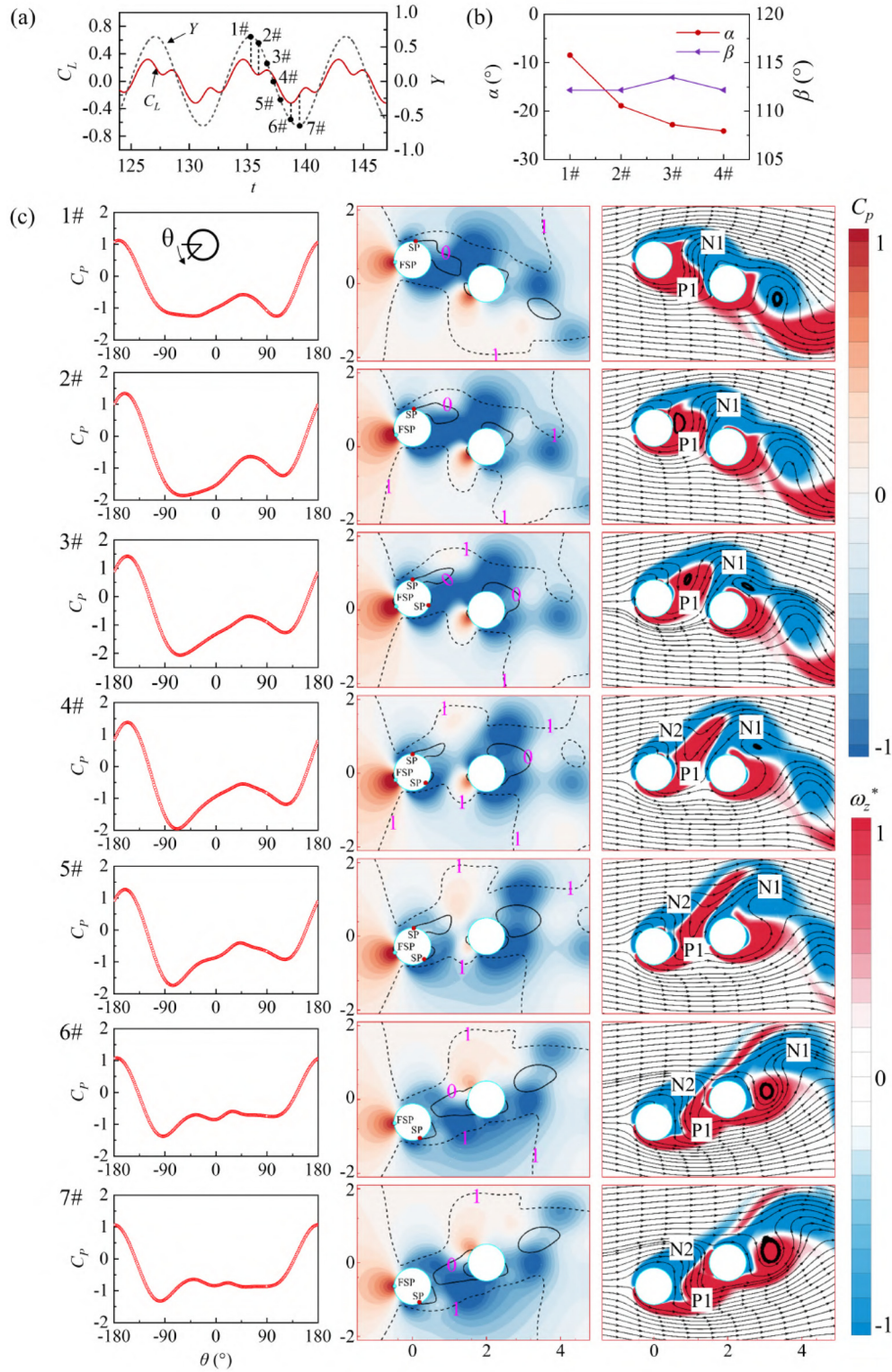


FIG. 21. (a) Lift coefficient and dimensionless amplitude, (b) variations of α and β in a half cycle of the displacement from 1# to 4#, and (c) the surface pressure coefficient and the contour of the surface pressure coefficient and the local vorticity at different times when $Re = 120$.

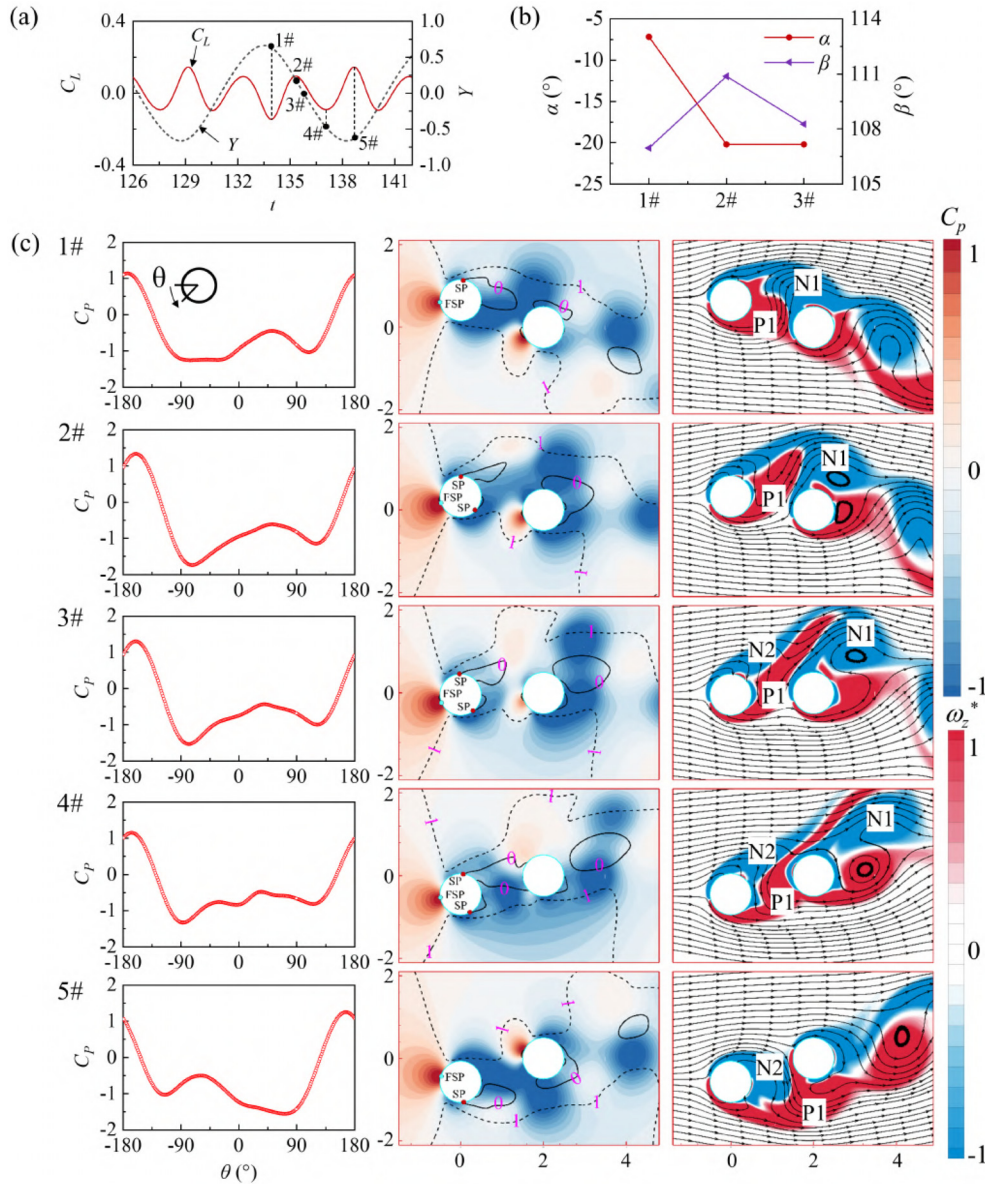


FIG. 22. (a) Lift coefficient and dimensionless amplitude, (b) variations of α and β in a half cycle of the displacement from 1# to 3#, and (c) the surface pressure coefficient and the contour of the surface pressure coefficient and the local vorticity at different times when $Re = 160$.

to 0. From the 4# to 7#, the growth of shear layer P1 generates a downward lift coefficient. At 6#, the shear layer P1 causes a complete downward velocity in the gap. The connection between vortex N1 and the UC is completely severed, the pressure on the upper surface of the UC increases to its maximum, and the downward lift coefficient generated by P1 reaches its maximum. At 7#, the enhancement of shear layer N2 leads to a decrease in pressure on the upper surface and lift coefficient.

At $Re = 160$, the amplitude of the third harmonic frequency of the lift coefficient exceeds the amplitude of the fundamental vortex shedding frequency. As shown in Fig. 22(b), the angle between the front stagnation point and the boundary layer separation point is

further reduced compared to that observed when $Re = 120$. At 1# in Fig. 22(c), the UC leaves the positive maximum displacement position. The vortex N1 causes an upward flow velocity in the gap, and the positive shear layer P1 moves to the rear of the UC with the water flow. The time-history curves in Fig. 22(a) show that C_L is minimum at this instance. From 1# to 2#, the shear layer P1 begins to cut off the connection between vortex N1 and the UC but is not destroyed. The separation point of the boundary layer on the lower surface moves downward, resulting in a decrease in the overall pressure on the lower surface of the UC. From 2# to 4#, the flow velocity in the gap turns downward, and the separation point of the lower boundary layer

gradually moves downward. The pressure on the lower surface is still lower than that on the upper surface, and the lift coefficient gradually decreases with the variation of vortex P1. At 4#, the connection between vortex N1 and the UC is completely severed, causing an increase in C_L as the remaining shear layer N2 changes direction in the gap. Figures 21 and 22 show that after the vortex is cut off by the shear layer in the gap, the growth of the remaining shear layer in the gap primarily controls the change in lift coefficient. This remaining shear layer acts like a switch, and the variation in the lift coefficient depends on its position in the displacement curve. This behavior differs from that of the third harmonic lift caused by the 2T pattern.

VI. CONCLUSIONS

In the present work, two-dimensional numerical simulations are carried out to study the influence of a fixed DC on the FIV of an elastically supported UC. The simulations are performed for a range of Re from 50 to 170 and a range of L/D from 1.25 to 3. The influence of L/D and Re on the FIV of the UC is investigated in detail. The main conclusions are summarized as follows:

- There is a significant impact of L/D and Re on the wake flow regime. Two distinct flow regimes, namely, the steady flow and alternating attachment, have been observed. Steady flow occurs in the low Re regime. The Re range for the steady flow regime decreases with increasing L/D . With increase in Re or L/D , the flow field transitions from the steady flow regime to an alternating attachment regime, which comprises the largest area in the $L/D - Re$ map.
- Various vortex shedding patterns are observed behind the tandem cylinders due to the hindrance of the DC on the vortex shedding of the UC. At $L/D = 1.25$, two vortex shedding patterns, 2C and aperiodic, are observed. For L/D between 1.5 and 1.75, four different vortex shedding patterns are observed: 2S, 2C, 2P, and aperiodic. At $L/D = 2$, three different vortex shedding patterns, 2S, 2C, and 2P, are observed. When L/D is greater than 2, only the 2S and 2C patterns are observed.
- After the UC starts vibrating, the interference effect of the DC at a small L/D slows down the increase rate of ϕ_{rms} between C_L and Y . As a result, the lift of the UC continuously promotes the increment of amplitude at small values of L/D . When L/D lies between 1.25 and 1.75, as the velocity increases, the ϕ_{rms} remains less than 45° , and the corresponding vibration characteristic of the UC is characterized as interference galloping. The lock-in frequency of the UC increases with increasing L/D but is smaller than the natural frequency of the UC. When $L/D \geq 2$, the vibration characteristics of the UC show extended VIV. In this vibration regime, the lock-in interval of the cylinder is significantly larger than that of a single cylinder, and the amplitude of the lock-in region gradually decreases with increasing L/D .
- The hindering effect of the DC on the vortex shedding of the UC results in variations in the shear layer in the gap, acting like a switch and altering the distribution of C_p on the UC surface. When the L/D value lies between 1.25 and 2, the third harmonic frequency of the C_L of the UC increases with increasing L/D . Moreover, at $L/D = 2$, the amplitude of the third harmonic frequency component will exceed that of the fundamental frequency component of C_L .

The findings of this study will allow us to better understand vibration reduction in tandem cylindrical structures and lead to efficient design of flow-induced energy harvesters.

ACKNOWLEDGMENTS

This work was supported by the National Natural Science Foundation of China (Grant No. 52277227), the Science and Technology Research & Development Joint Foundation of Henan Province-Young Scientists (Grant No. 225200810099), and the Program for Science & Technology Innovation Talents in Universities of Henan Province (Grant No. 23HASTIT010).

AUTHOR DECLARATIONS

Conflict of Interest

The authors have no conflicts to disclose.

Author Contributions

Junlei Wang: Conceptualization (equal); Funding acquisition (equal); Investigation (equal); Project administration (equal); Supervision (equal); Writing – original draft (equal); Writing – review & editing (equal). **Shenfeng Li:** Data curation (equal); Formal analysis (equal); Investigation (equal); Methodology (equal); Validation (equal); Visualization (equal); Writing – original draft (equal). **Daniil Yurchenko:** Conceptualization (equal); Writing – review & editing (equal). **Hongjun Zhu:** Conceptualization (equal); Writing – review & editing (equal). **Chandan Bose:** Conceptualization (equal); Formal analysis (equal); Investigation (equal); Methodology (equal); Supervision (equal); Writing – original draft (equal); Writing – review & editing (equal).

DATA AVAILABILITY

The data that support the findings of this study are available from the first author/corresponding author upon reasonable request.

REFERENCES

- ¹L. Chen, Y. Dong, and Y. Wang, "Flow-induced vibration of a near-wall circular cylinder with a small gap ratio at low Reynolds numbers," *J. Fluids Struct.* **103**, 103247 (2021).
- ²G. Hu, J. Wang, Z. Su, G. Li, H. Peng, and K. Kwok, "Performance evaluation of twin piezoelectric wind energy harvesters under mutual interference," *Appl. Phys. Lett.* **115**, 073901 (2019).
- ³F. Zafar and M. M. Alam, "A low Reynolds number flow and heat transfer topology of a cylinder in a wake," *Phys. Fluids* **30**, 083603 (2018).
- ⁴Z. Zhang and C. Ji, "Spacing effect on the vortex-induced vibrations of near-wall flexible cylinders in the tandem arrangement," *Phys. Fluids* **34**, 097123 (2022).
- ⁵M. Zhang, Y. Song, A. Abdelkefi, H. Yu, and J. Wang, "Vortex-induced vibration of a circular cylinder with nonlinear stiffness: Prediction using forced vibration data," *Nonlinear Dyn.* **108**, 1867–1884 (2022).
- ⁶C. H. Williamson and R. Govardhan, "Vortex-induced vibrations," *Annu. Rev. Fluid Mech.* **36**, 413–455 (2004).
- ⁷J. Wang, S. Gu, C. Zhang, G. Hu, G. Chen, K. Yang, H. Li, Y. Lai, G. Litak, and D. Yurchenko, "Hybrid wind energy scavenging by coupling vortex-induced vibrations and galloping," *Energy Convers. Manage.* **213**, 112835 (2020).
- ⁸J. Wang, C. Zhang, M. Zhang, A. Abdelkefi, H. Yu, X. Ge, and H. Liu, "Enhancing energy harvesting from flow-induced vibrations of a circular cylinder using a downstream rectangular plate: An experimental study," *Int. J. Mech. Sci.* **211**, 106781 (2021).

- ⁹G. R. S. Assi, J. R. Meneghini, J. A. P. Aranha, P. W. Bearman, and E. Casaprima, "Experimental investigation of flow-induced vibration interference between two circular cylinders," *J. Fluids Struct.* **22**, 819–827 (2006).
- ¹⁰H. H. Khan, M. D. Islam, Y. Y. Fatt, I. Janajreh, and M. M. Alam, "Flow-induced vibration on two tandem cylinders of different diameters and spacing ratios," *Ocean Eng.* **258**, 111747 (2022).
- ¹¹G. R. S. Assi, P. W. Bearman, N. Kitney, and M. Tognarelli, "Suppression of wake-induced vibration of tandem cylinders with free-to-rotate control plates," *J. Fluids Struct.* **26**, 1045–1057 (2010).
- ¹²G. R. Assi, P. Bearman, and J. Meneghini, "On the wake-induced vibration of tandem circular cylinders: The vortex interaction excitation mechanism," *J. Fluid Mech.* **661**, 365–401 (2010).
- ¹³A. Bakhtiari, M. Zeinoddini, H. Ashrafipour, and V. Tamimi, "The effect of end conditions on the flow-induced vibration of circular cylinders in tandem arrangements," *Appl. Ocean Res.* **105**, 102406 (2020).
- ¹⁴R. Tang, Y. Gu, X. Mi, D. Yurchenko, F. Xu, W. Xu, X. Liu, and J. Wang, "Numerical analysis of wiv phenomenon with two in-series cylinders: WIV suppression and energy harvesting," *Ocean Eng.* **262**, 112154 (2022).
- ¹⁵H. Ping, Y. Cao, K. Zhang, Z. Han, D. Zhou, H. Zhu, and Y. Bao, "Vortex-induced vibrations of two rigidly coupled circular cylinders in tandem arrangement," *Ocean Eng.* **263**, 112316 (2022).
- ¹⁶H. Zhu and K. Wang, "Wake adjustment and vortex-induced vibration of a circular cylinder with a C-shaped plate at a low Reynolds number of 100," *Phys. Fluids* **31**, 103602 (2019).
- ¹⁷B. Qin, M. M. Alam, and Y. Zhou, "Two tandem cylinders of different diameters in cross-flow: Flow-induced vibration," *J. Fluid Mech.* **829**, 621–658 (2017).
- ¹⁸Z. Hu, J. Wang, and Y. Sun, "Flow-induced vibration of one-fixed-one-free tandem arrangement cylinders with different mass-damping ratios using wind tunnel experiment," *J. Fluids Struct.* **96**, 103019 (2020).
- ¹⁹I. Borazjani and F. Sotiropoulos, "Vortex-induced vibrations of two cylinders in tandem arrangement in the proximity-wake interference region," *J. Fluid Mech.* **621**, 321–364 (2009).
- ²⁰H. Zhu, S. Wang, T. Zhou, and Z. Shao, "Wake evolution and vortex structure characteristics of flow over two tandem semi-circular cylinders with flat surfaces facing each other," *Phys. Fluids* **33**, 113604 (2021).
- ²¹J. Tu, Z. He, X. Tan, G. Wang, J. Xu, and Y. Xu, "Study for the cross-flow coupling mechanism of tandem cylinder groups at low Reynolds number," *Ocean Eng.* **260**, 112004 (2022).
- ²²V. D. Duong, V. D. Nguyen, V. T. Nguyen, and I. L. Ngo, "Low-Reynolds-number wake of three tandem elliptic cylinders," *Phys. Fluids* **34**, 043605 (2022).
- ²³N. Hosseini, M. Griffith, and J. Leontini, "Flow-induced vibrations in long rows of cylinders and their links to convective instabilities," *Int. J. Heat Fluid Flow* **94**, 108922 (2022).
- ²⁴D. Sumner, "Two circular cylinders in cross-flow: A review," *J. Fluids Struct.* **26**, 849–899 (2010).
- ²⁵L. Zhang, H. Dai, A. Abdelkefi, and L. Wang, "Improving the performance of aeroelastic energy harvesters by an interference cylinder," *Appl. Phys. Lett.* **111**, 073904 (2017).
- ²⁶L. Zhang, H. Dai, A. Abdelkefi, and L. Wang, "Experimental investigation of aerodynamic energy harvester with different interference cylinder cross-sections," *Energy* **167**, 970–981 (2019).
- ²⁷C. Williamson *et al.*, "The existence of two stages in the transition to three-dimensionality of a cylinder wake," *Phys. Fluids* **31**, 3165 (1988).
- ²⁸C. Zhou, R. So, and K. Lam, "Vortex-induced vibrations of an elastic circular cylinder," *J. Fluids Struct.* **13**, 165–189 (1999).
- ²⁹Y. Bao, C. Huang, D. Zhou, J. Tu, and Z. Han, "Two-degree-of-freedom flow-induced vibrations on isolated and tandem cylinders with varying natural frequency ratios," *J. Fluids Struct.* **35**, 50–75 (2012).
- ³⁰U. Ali, M. Islam, and I. Janajreh, "Heat transfer and wake-induced vibrations of heated tandem cylinders with two degrees of freedom: Effect of spacing ratio," *Phys. Fluids* **34**(11), 113612 (2022).
- ³¹M. A. Stremmer, A. Salmanzadeh, S. Basu, and C. H. Williamson, "A mathematical model of 2P and 2C vortex wakes," *J. Fluids Struct.* **27**, 774–783 (2011).
- ³²B. Dielen and H. Ruscheweyh, "Mechanism of interference galloping of two identical circular cylinders in cross flow," *J. Wind Eng. Ind. Aerodyn.* **54–55**, 289–300 (1995).
- ³³J. Chunning, C. Weilin, H. Jilu, and X. Wanhai, "Numerical investigation on flow-induced vibration of two cylinders in tandem arrangements and its coupling mechanisms," *Chin. J. Theor. Appl. Mech.* **46**, 862–870 (2014).
- ³⁴W. Chen, C. Ji, M. M. Alam, D. Xu, H. An, F. Tong, and Y. Zhao, "Flow-induced vibrations of a D-section prism at a low Reynolds number," *J. Fluid Mech.* **941**, A52 (2022).
- ³⁵A. Bokaian and F. Geoola, "Proximity-induced galloping of two interfering circular cylinders," *J. Fluid Mech.* **146**, 417–449 (1984).
- ³⁶X. Wu, F. Ge, and Y. Hong, "A review of recent studies on vortex-induced vibrations of long slender cylinders," *J. Fluids Struct.* **28**, 292–308 (2012).